GA-A24853

IMPLICATIONS OF WALL RECYCLING AND CARBON SOURCE LOCATIONS ON CORE PLASMA FUELING AND IMPURITY CONTENT IN DIII-D

by

M. GROTH,[£] G.D. PORTER,[£] J.A. BOEDO,[§] N.H. BROOKS,
M.E. FENSTERMACHER,[£] R.J. GROEBNER, C.J. LASNIER,[£]
W.M. MEYER,[£] R.A. MOYER,[§] L.W. OWEN,[¶] T.W. PETRIE,
M.E. RENSINK,[£] D.L. RUDAKOV,[§] G. WANG,[‡]
J.G. WATKINS,[°] N.S. WOLF,[£] and L. ZENG[‡]

[£]Lawrence Livermore National Laboratory, Livermore, California
[§]University of California, San Diego, California
[¶]Oak Ridge National Laboratory, Oak Ridge, Tennessee
[‡]University of California, Los Angeles, California
[°]Sandia National Laboratory, Albuquerque, California

DISCLAIMER

GA-A24853

IMPLICATIONS OF WALL RECYCLING AND CARBON SOURCE LOCATIONS ON CORE PLASMA FUELING AND IMPURITY CONTENT IN DIII-D

by

M. GROTH, G.D. PORTER, J.A. BOEDO, N.H. BROOKS,
M.E. FENSTERMACHER, R.J. GROEBNER, C.J. LASNIER,
W.M. MEYER, R.A. MOYER, L.W. OWEN, T.W. PETRIE,
M.E. RENSINK, D.L. RUDAKOV, G. WANG,
J.G. WATKINS, N.S. WOLF, and L. ZENG

NOVEMBER 2004

Implications of Wall Recycling and Carbon Source Locations on Core Plasma Fueling and Impurity Content in DIII-D

M. Groth,[1] G.D. Porter,[1] J.A. Boedo,[2] N.H. Brooks,[3] M.E. Fenstermacher,[1] R.J. Groebner,[3] C.J. Lasnier,[1] W.M. Meyer,[1] R.A. Moyer,[2] L.W. Owen,[4] T.W. Petrie,[3] M.E. Rensink,[1] D.L. Rudakov,[2] G. Wang,[5] J.G. Watkins,[6] N.S. Wolf,[1] L. Zeng[5]

[1]Lawrence Livermore National Laboratory, Livermore, California, USA
[2]University of California, San Diego, California, USA
[3]General Atomics, San Diego, California, USA
[4]Oak Ridge National Laboratory, Oak Ridge, Tennessee, USA
[5]University of California, Los Angeles, California, USA
[6]Sandia National Laboratory, Albuquerque, California, USA

e-mail contact of main author: groth@fusion.gat.com

Abstract. Measurement and modeling of the 2-D poloidal D_α intensity distribution in DIII-D low and medium density L-mode and ELMy H-mode plasmas indicate that hydrogen neutrals predominantly fuel the core from the divertor X-point region. The 2-D distribution of neutral deuterium and low-charge-state carbon were measured in the divertor and the high-field side midplane scrape-off layer (SOL) using tangentially viewing cameras. The emission in the high-field SOL at the equatorial plane was found to be three to four orders of magnitude lower than at the strike points in the divertor, suggesting a strong divertor particle source. Modeling using the UEDGE/DEGAS codes predicted the poloidal fueling distribution to be dependent on the direction of the ion $\mathbf{B}x\nabla B$ drift. In plasmas with the $\mathbf{B}x\nabla B$ drift into the divertor stronger fueling from the inner divertor than from the outer is predicted, due to a lower-temperature and higher-density plasma in the inner leg. UEDGE simulations with carbon produced by both physical and chemical sputtering at the divertor plates and walls only are in agreement with a large set of diagnostic data. The simulations indicate flow reversal in the inner divertor that augments the leakage of carbon ions from the divertor into the core.

1. Introduction and Motivation

The poloidal distribution of the hydrogen and impurity particle sources in tokamaks is an important ingredient in the formation of the H-mode pedestal [1], and in achieving the projected performance in future fusion devices [2]. Divertors were introduced in fusion devices to move the principal particle sources away from the main chamber to the remote region of the divertor, because main chamber wall impurities can significantly increase the core impurity content, cool the core pedestal region, and thus limit the overall plasma performance. The screening efficiency of the scrape-off layer (SOL) plasma, i.e. the probability of impurities sputtered at plasma facing components being ionized in the SOL plasma and prevented from penatrating to the core, is higher for divertor sources than main chamber sources. In current devices core density control using divertor pumping is easier to achieve with divertor sources compared to main chamber sources. Reducing divertor neutral leakage by increasing divertor closure has led to a reduction in the main chamber pressure, and hence hydrogen charge-exchange (CX) fluxes to the main walls in some devices [3,4,5]. The central impurity levels are not strongly affected by changes to the divertor geometry [6], or are governed by both divertor and main wall sources [7,8]. Increased plasma-main wall contact during Edge-Localized Modes (ELMs) [9] and intermittent transport events [10,11] are of concern for next-step devices because of main chamber sources and the longevity of the first wall. This paper focuses on well-diagnosed experiments in DIII-D, coupled to numerical simulations, that better quantify divertor and main wall sources. The principal measurements in this paper are 2-D poloidal distributions of D_α, CII (514 nm), and CIII (465 nm), inferred from tangentially viewing Charge-Injection Device (CID)

cameras [12,13]. The poloidal coverage of these cameras spans the region of the lower and upper divertor, and the high-field main scrape-off layer (SOL) ≈0.5 m above and below the device midplane (Fig. 1). Other diagnostics include vertically and tangentially viewing photomultiplier (PMT) arrays [14], Langmuir probes (LPs) embedded in the divertor target plates [15], a reciprocating Langmuir probe (RCP) system at the outer midplane [16], a reflectometer system at the outer midplane [17], and a Thomson scattering system in the core and main SOL region [18]. The intensity distributions of the D_α, CII, and CIII emission were simulated using the edge fluid code UEDGE [19] and neutral transport code DEGAS [20]. Neutral transport and core plasma fueling rates, as well as impurity sources and transport rates were extracted from the code simulations. Detailed comparisons of the experimental results with the transport models are presented for the following operational regimes: (i) low-to-medium density L-mode discussed in Sec. 2, and (ii) medium-to-high density ELMy H-mode addressed in Sec. 3. These results are summarized in Sec.4.

FIG. 1. *Subset of the DIII-D edge diagnostic system as described in section 1. The black rectangles indicate the fields-of-view of the tangential cameras for which 2-D poloidal intensity distributions were calculated. The seperatrix and the 6 cm flux surface of the magnetic configuration is shown for the L-mode reference discharge 119919 at 3s. Other discharge parameters include total heating power P_{tot} = 900 kW, toroidal field B_T = 2.0 T, and plasma current I_p = 1.1 MA*

2.   Results in Low-to-Medium Density L-mode Plasmas

2.1.   Methodology and Experimental Measurements

Analyses of DIII-D plasmas with the full set of tangential cameras were performed in low-confinement mode (L-mode) for three different core plasma densities: n_e = 2.6x10^{19} m^{-3} (n_e/n_{GW} = 0.23), n_e = 3.1x10^{19} m^{-3} (n_e/n_{GW} = 0.29), and n_e = 4.1x10^{19} m^{-3} (n_e/n_{GW} = 0.37), where n_{GW} is the Greenwald density [21]. The plasma configuration was a lower single-null (LSN) with the ion $\mathbf{B}$x∇B drift direction toward the lower divertor (Fig. 1). To optimize diagnostic spatial resolution of the divertor plasma, the inner and outer strike points (ISP and OSP, respectively) were swept across the LPs and the view chords of the lower vertical PMT arrays. During the strike point sweep the separatrix-to-wall gaps at the inner and outer tokamak midplane were maintained at 12.5 cm and 9 cm. In this configuration the first flux surface that is limited by the main chamber wall was at the upper baffle limiter, 7 cm radially outward from the separatrix when mapped to the outer midplane (OMP flux surface).

The electron temperature, T_e, measured with LPs near the OSP indicated that the outer divertor plasma went from an attached to a detached state, as the core plasma density was raised from the lowest to the highest density. For the lowest core plasma density, $T_{e,OSP}$ ~ 25 eV. Between the intermediate and highest density the peak ion saturation current, I_{sat}, decreased significantly, while T_e fell below 5 eV. The ion saturation current to the inner divertor target decreased as the core density was raised from the lowest to the intermediatel evel, and T_e ≤ 8 eV at the inner target for all densities, suggesting that the inner divertor plasma was, in general, at least partially detached.
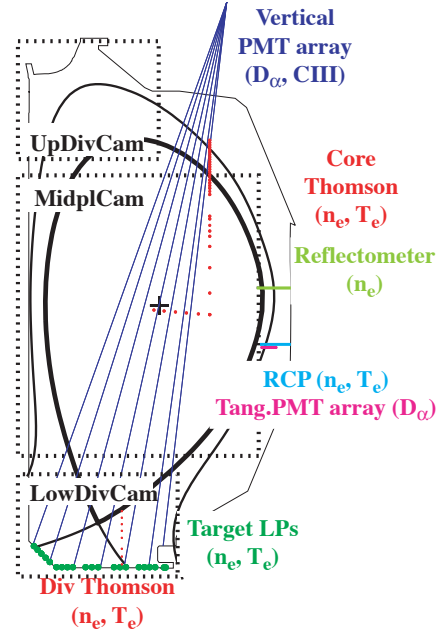
The intensity distributions of deuterium neutral and carbon ion emission in the lower divertor indicated that, at the lowest density, the outer divertor leg was fully attached, whereas the inner leg was at least partially detached for all three densities. This was consistent with the LP measurements. The D_α and D_γ emissions in the inner divertor leg peaked strongly at the target [Fig. 2(b)], while CII and CIII emission were only observed in the inner SOL near the divertor X-point. In the outer divertor leg the D_α and D_γ emission were at least a factor five lower than in the inner leg, whereas the CII and CIII emission peaked strongly at the OSP. The D_α and D_γ emission extended farther into the inner divertor plasma toward the X-point at intermediate density, and peaked at the OSP at the highest density. With increasing density the CII and CIII emission moved closer to the divertor X-point in the inner leg, and off the OSP in the outer leg, until, at the highest density, a MARFE formed inside the separatrix.

The D_α, CII, and CIII intensity distributions measured in the high-field side SOL in the region 0.5 m above and below the equatorial plane, peaked near the lower divertor X-point [Fig. 2(a)], suggesting that the particle sources were located in the divertor region. If the inner wall was the dominant source of particles, a more uniform or poloidally symmetric intensity distribution would be expected. The D_α peak emissivity at the ISP dropped by more than two orders of magnitude relative to the inner midplane region, while the ratio of the CIII emission in the inner divertor leg near the
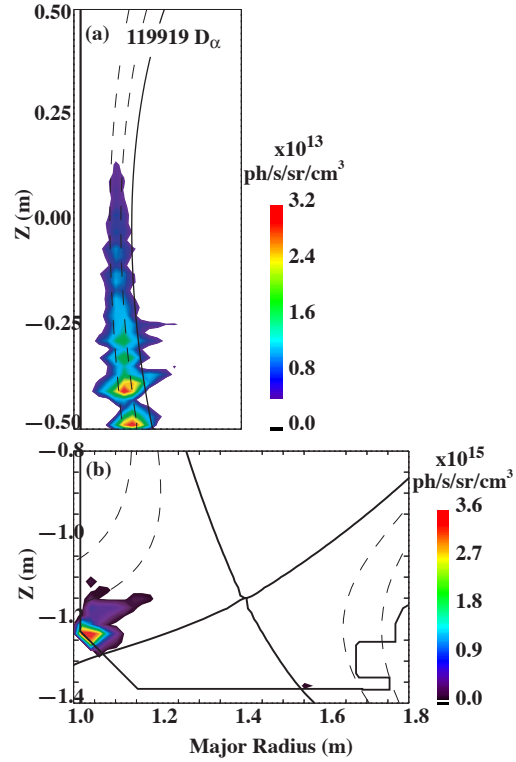

FIG. 2. Experimental D_α intensity distribution in the high-field midplane SOL (a) and lower divertor (b) obtained in low density L-mode discharge 119919. The separatrix is shown in solid black, and the 2 cm and 4 cm flux surfaces are shown in dashed black. Note that two seperate scales for the emissivities of the inner midplane and divertor region are used.
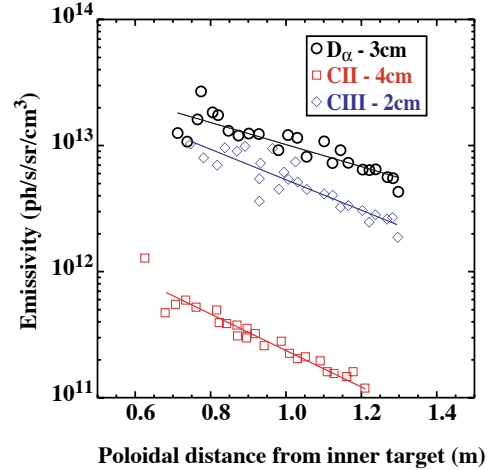
FIG. 3. Inner midplane poloidal emissivity profiles obtained in low density L-mode discharges for D_α (3 cm OMP flux surface), CII (4 cm OMP flux surface), and CIII (2 cm OMP flux surface). Fits to the experimental data using exponential functions are indicated by the solid lines.

X-point to the emission at the midplane was only a factor 5-10. From the region around $Z = -0.5$ m the poloidal decrease of the emission was nearly exponential along the flux surfaces. The measured poloidal fall-off lengths were 0.5 m (D_α), 0.3 m (CII), and 0.4 m (CIII), showing little dependence on core density (Fig. 3 and Table I). Radially, the CII and CIII

emission profiles peaked at the 3 cm and 1–2 cm flux surfaces, respectively. This is consistent, within the error bars of the measurement and flux surface mapping, with electron temperatures of 10 eV and 15-20 eV, measured at the same two flux surfaces with the outer midplane reciprocating probe.

2.2. Poloidal Core Fueling Profiles and Carbon Transport Using UEDGE/DEGAS

Simulations of an L-mode plasma at $n_e = 2.1 \times 10^{19} m^{-3}$ ($n_e/n_{GW} = 0.20$) using the UEDGE and DEGAS codes showed that fueling through the inner divertor X-point region is the dominant core plasma fueling mechanism. The simulations were done for a LSN configuration very similar to the experiment except at slightly higher triangularity. The calculated intensity distribution of the D_α, CII, and CIII emission in the divertor and main SOL matched the measured spatial distribution and absolute magnitude within a factor of 2-3 Core plasma fueling, carbon sources, and carbon transport from the wall source to the core were extracted from the codes. The fluid edge code UEDGE calculated the 2-D plasma solution using a classical transport description in the parallel **B** direction, including the ion $\mathbf{B} \times \nabla \mathbf{B}$ and $\mathbf{E} \times \mathbf{B}$ drift terms [22], and a purely diffusive radial transport model with spatially constant diffusivities for the region $0.94 \leq \Psi_N \leq 1.15$ These (anomalous) diffusivities were obtained by matching the calculated n_e and T_e profiles in the core and the main SOL with those measured by the core Thomson system: $D_\perp = 0.2 \ m^2/s$, and $\chi_e = \chi_i = 0.8 \ m^2/s$. In UEDGE, ions were allowed to recycle as neutrals both at the divertor plates and at the radially outermost grid boundary with a

TABLE I Characteristic poloidal fall-off length of the emission profiles measured in the inner midplane SOL region (in m). All plasmas were in LSN configuration with BxVB drift into lower divertor.

	L-mode			ELMy H-mode	
$\langle n_e \rangle$ (10^{19} m^{-3})	2.6	3.1	4.1	4.8	9.5
n/n_{GW}	0.24	0.29	0.37	0.4	0.7
$L_{pol,D\alpha}$ (m)	0.5	0.4	0.4	0.1	0.4
$L_{pol,CII}$ (m)	0.3	0.4	0.3	0.1	–
$L_{pol, CIII}$ (m)	0.3	0.3	0.5	0.6	0.5

recycling coefficient of unity. Neutrals striking the target plates, the private flux boundary, and the outermost grid boundary including the area up to 20 cm poloidally off the inner and outer plates were returned isotropically. Further poloidally upstream from the targets, 5% of the neutrals crossing the UEDGE grid boundary were removed from the domain. Carbon neutrals were produced by physical and chemical sputtering at the target plates using yields obtained from the Toronto database [23]. The ion transport of each charge state was modeled using a force balance equation [24]. The transport of neutrals from the divertor target plates to the main chamber, including reflections at the wall and CX scattering, were modeled using the Monte-Carlo code DEGAS in realistic DIII-D geometry [25,26]. For the halo plasma region, i.e., the region between the UEDGE numerical domain and the DIII-D wall, constant n_e, T_e, and T_i of 0.5 times the value of the UEDGE outermost grid cells were used. This assumption was consistent with reciprocating Langmuir and profile reflectometer n_e and T_e measurements in the far SOL at the outer midplane.

Many aspects of the simulated D_α emission agreed with the measurements in the lower divertor, and in both inner and outer midplane SOL. In the lower divertor the D_α emission calculated from DEGAS peaked at the ISP, and was ≈ 3 orders of magnitude lower in the high-field SOL at the tokamak midplane. In the inner midplane SOL the simulated D_α emission decreased over a poloidal scale length of 0.15 m, a factor three shorter than that measured. In the outer main SOL the D_α emission profile measured by the tangential PMT array near the midplane was well reproduced using a wall pumping coefficient of 0.36 in DEGAS. With zero wall pumping, the codes overestimated the D_α emission by a factor 2-5. This indicated that additional recycling of ions at the main chamber wall near the outer midplane was not required to fit the PMT data.

The poloidal distribution of the neutral flux into the core plasma calculated by DEGAS for the low density case suggests that approximately 70% of the neutrals that cross the separatrix do so in the divertor region (Fig. 4). The remaining 30% of the core fueling arises from neutral leakage out of the divertor. The DEGAS simulation showed that the divertor X-point region extends approximately 2-3 CX mean free paths, approximately 20 cm, above the magnetic X-point in the inner divertor plasma, resulting in core fueling from the inner leg being approximately twice asstrong as from the outer leg. This is primarily due to the significantly colder plasma in the inner divertor, which results inless ionization of neutrals in the inner divertor compared to that in the outer.

The UEDGE simulations reproduced the measured, spatially non-uniform CII and CIII distribution around the inner midplane, indicating that the divertor walls provide sufficient source to explain the upstream carbon density. Here, the divertor walls are
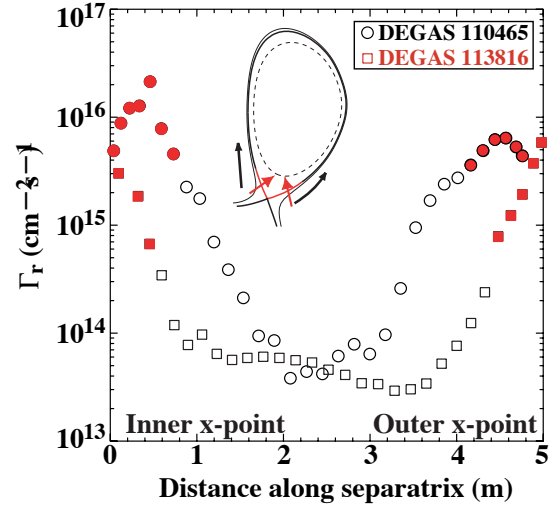

FIG. 4. *Calculated neutral flux across the separatrix from DEGAS as a function of poloidal distance along the separatrix for L-mode (circles) and ELMy H-mode (squares). The poloidal distance is measured from the inboard side of the X-point over the top of the plasma to the outboard side. Fueling through the divertor x-point as indicated by the closed symbols contributed 75% (L-mode) and 90% (ELMy H-mode) to the total divertor fueling. The open symbols represent fueling due to divertor neutral leakage.*

defined as the outermost UEDGE boundary in the SOL, extending from the target plates *to about 20 cm above the X-point*. Using chemical sputtering yields published in [23] the calculations of the total radiation in the core and SOL, the target heat flux profile, and the line-integrated CIII emission from the vertical PMT array all matched the measurements. Chemical sputtering of carbon was a significant source along the UEDGE outermost boundary 20-30 cm upstream from the inner targets and at the interface to the private flux region. Carbon (physically and chemically) sputtered from the target plates was predominately redeposited onto the plates.

The UEDGE simulations showed complex carbon transport dynamics in which impurity **ExB** drifts and drag on fuel ions both play an important role. Carbon is swept from the private flux region to the inner divertor leg due to **ExB** drifts caused by the radial electric field near the separatrix. Flow reversal in the far-SOL region of the inner divertor leg allows carbon to drift upstream due to ∇T_i forces, while in the region near the separatrix carbon is swept towards the target plate by drag from the background plasma flow. Above $Z = -0.8$ m, the ion temperature gradient force on the carbon ions exceeds the frictional drag from the background plasma, and carbon drifts into the inner main SOL. In the UEDGE simulations the poloidal fall-off lengths for CII (0.5 m) and CIII (0.9 m) are typically a factor two higher than those measured, indicating the existence of either stronger temperature gradients or lower background flows in the simulation of the main SOL than in the experiment.

3. Analysis in Medium-to-High Density ELMy H-mode Plasmas

3.1. Emission Distribution Profiles in Medium-Density LSN, DN, and USN Plasmas

Measurements of poloidally non-uniform D_α, CII, and CIII intensity profiles were also obtained in the inner midplane SOL for medium-density ELMy H-mode plasmas with several magnetic configurations and both ion **B**x∇B drift directions, all showing the maximum

emission nearest the divertor X-point region. For similar pedestal parameters ($n_{e,ped}$ = 4.5×10^{19} m^{-3}, $T_{e,ped}$ = 450–900 eV) three plasma configurations with the ion $\mathbf{B}x\nabla B$ drift into the upper divertor were established (Fig. 5 insert): an upper single-null (USN), double-null (DN), and lower single-null (LSN) configuration. The SN plasmas had a secondary X-point inside the vacuum vessel, with the two separatrices separated by ±4 cm measured at the outer midplane (OMP). The same three magnetic configurations were repeated with the reversed toroidal field direction, the ion $\mathbf{B}x\nabla B$ into the lower divertor.

For plasmas with the $\mathbf{B}x\nabla B$ drift into the upper divertor, the peak D_α emission in the inner midplane SOL was measured in the region closest to the primary X-point, and close to both X-points in the DN case (Fig. 5). The emission profiles were time-averaged over 10ms, hence over a couple of ELMs. Previously, it was shown that the emission is dominated by the emission between ELMs [27]. The peak D_α emissivity in the divertor with the X-point at the lowest value of poloidal flux (primary divertor) was ≈ 2 orders of magnitude higher than in the inner midplane SOL, and about one to two orders of magnitude higher
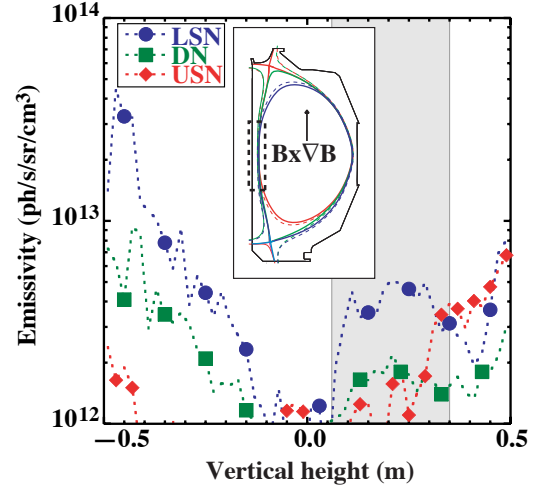

FIG. 5. *Comparison of the D_α emissivity in the inner midplane SOL as a function of vertical height around the equatorial plane for ELMy H-mode discharges in LSN, DN, and USN with the ion $\mathbf{B}x\nabla B$ drift into the upper divertor. Other plasma operational parameters include P_{NBI} = 5.5 MW, H_{89} ~ 2, B_T = 2.0 T, I_p = 1.3 MA, and n_e = $5.2\times10^{19}m^{-3}$ (n_e/n_{GW} = 0.4). The shaded area indicates a region affected by reflections of light at the outer wall. Insert: LSN, DN, and USN equilibria. The region over which the vertical profiles were calculated is indicated by the dashed rectangle*

than in the secondary divertor. In the inner SOL, the emission decreases by another order of magnitude from the divertor X-point region (Z = ±0.5 m) to the midplane (Z = 0) over a characteristic length of 10-20 cm.

In comparison, the peak CII emission in the primary divertors was ≈ 2 to 3 orders of magnitude higher than in the inner midplane SOL and in the secondary divertors. In the inner midplane SOL the CII emission decreased from the primary divertor X-point toward the midplane over a poloidal scale length of 10–20 cm, along the 3 cm OMP flux surface. The presence of a secondary X-point inside the vacuum vessel gave rise to plasma-wall interaction in the secondary divertors, and significant D_α and carbon emission were observed mainly in the outer divertor leg, independent of the magnetic configuration and ion $\mathbf{B}x\nabla B$ drift direction. This is consistent with the assertion that the particle loss through the outboard separatrix is larger than through the inboard separatrix [28].

The effect of $\mathbf{E}x\mathbf{B}$ induced particle flow in the private flux region was observed in the divertor D_α emission profiles: in configurations with the ion $\mathbf{B}x\nabla B$ drift into the primary divertor the profiles peaked by a factor of 3 in the inner divertor leg relative to the outer leg, while in the configurations with the ion $\mathbf{B}x\nabla B$ drift pointing out of the primary divertor, the peak D_α emission was similar in magnitude in the inner and outer divertor leg.

The spatial D_α distribution measured in the lower divertor for the two $\mathbf{B}x\nabla B$ drift directions was consistently reproduced in UEDGE only when the $\mathbf{B}x\nabla B$ and $\mathbf{E}x\mathbf{B}$ terms were included in the simulations. This emphasizes the importance of incorporating the drifts in the modeling. Here, only the plasma state between ELMs was addressed in the modeling. The spatially constant diffusivities used for the radial transport to match the experimental outer midplane n_e and T_e profiles were lower than for the L-mode case, i.e., $D_\perp$ = 0.0875 m^2/s, χ_e = χ_i = 0.35 m^2/s. Unity recycling was assumed for ions striking the divertor plate, the

boundary to the private flux region, and the radially outermost boundary. Finite wall pumping of neutral particles was permitted via the neutral albedo: 2% of all neutrals striking the target plate, or crossing the interface to the private flux region were removed. Along the radially outermost boundary, 2% of all neutrals were removed for the region from the targets up to 10 cm upstream, and 5% elsewhere. Carbon was introduced by physical and chemical sputtering at the target, and chemical sputtering at the radial outermost UEDGE boundary.

The UEDGE simulations showed that, depending on the ion $\mathbf{B}x\nabla B$ drift direction, the $\mathbf{E}x\mathbf{B}$ induced particle flow in the private flux region can lead to asymmetries in the plasma conditions in the inner and outer divertor leg, which is in agreement with experimental observations. In LSN discharges with the ion $\mathbf{B}x\nabla B$ drift into the lower divertor (Case A), modeling showed a strong effect of the $\mathbf{E}x\mathbf{B}$ induced particle drifts in the private flux region, that is from outer to the inner divertor leg. This resulted in a higher-density and lower-temperature plasma in the inner leg, and thus higher D_α emission. In LSN discharges with the ion $\mathbf{B}x\nabla B$ drift out of the lower divertor (Case B), with reversed direction of the $\mathbf{E}x\mathbf{B}$ drifts, the magnitude of the calculated particle drifts is similar to those of Case A. The density and temperature profiles in the inner and outer divertor legs were more symmetric, and therefore also the D_α emission distribution. Both effects were experimentally observed in the D_α emission. These results, however, also indicate that particle drifts due to $\mathbf{E}x\mathbf{B}$ in the private flux region alone cannot explain the asymmetry of the plasma conditions in the inner and outer divertor legs, and that the interplay between the stronger particle loss across the outboard separatrix, the difference in connection lengths from the outboard midplane to the inner and outer divertor target plates, and the drifts in the divertor must be considered. In case A, flow reversal occurs mainly in the inner divertor leg, enhancing the leakage of carbon from this region into the main SOL. In case B, the code predicts a flow reversal region in the outer divertor leg, with lower carbon leakage as seen in Case A. Away from the divertor, UEDGE predicted a significantly stronger CII emission in the inner main SOL for Case A, which was not conclusively measured by the midplane camera. In both cases, the simulated CII emission decreases vertically toward the inner midplane, consistent with the experiment.

3.2. Emission Distribution Profiles in High-Density LSN Plasmas

In LSN ELMy H-mode discharges at higher density ($n_{e,ped} = 6.5 \times 10^{19}$ m^{-3}, $n_e/n_{GW} = 0.7$, $T_{e,ped} = 400$ eV) the measured D_α and CIII emission distribution in the inner midplane SOL remained peaked near the lower divertor X-point region, while their poloidal fall-off lengths increased to 40 cm and 50 cm, respectively, compared to the lower density ELMy H-mode cases. Both the D_α and CIII intensity distributions peaked radially at the 1 cm OMP flux surface, consistent with the local electron temperature at this flux surface of ~10 eV, measured by the reciprocating probe at the OMP. In the lower divertor, the measured D_α and D_γ emission peaked at the inner divertor target plate, and the peak D_α was approximately two orders of magnitude higher than that measured at the inner midplane. The observed CII and CIII emission in the lower divertor indicated that the plasma in the outer divertor leg was well attached, while in the inner divertor leg local maxima at the ISP and midway between the ISP and X-point were observed. Preliminary simulations of the spatial distribution of D_α and CIII in the lower divertor and inner midplane SOL using UEDGE are in agreement with the measurements, and the calculated poloidal fall-off length of CIII emission in the inner midplane SOL is 0.8 m.

4. Summary

Two-dimensional poloidal emission distributions from tangentially viewing camera measurements, coupled with UEDGE/DEGAS code simulations that reproduce these measurements and those from multiple other diagnostics, indicate that divertor recycling is the dominant particle source of the core plasma in DIII-D low-to-medium density L-mode plasmas. The same measurements obtained in ELMy H-mode plasmas of different magnetic configura-

tions and core plasma densities between 0.4 and 0.7 of the Greenwald density implied that also in this confinement regime divertor sources are the main sources for core plasma fueling and impurities. For a low density L-mode plasma, a large set of experimental data was simultaneously reproduced by the simulations, using a purely diffusive radial transport model in UEDGE. Core fueling and neutral leakage was calculated using the DEGAS code based on the UEDGE plasma solution. In the simulations particle recycling occurred predominantly at the divertor plates and walls, and not at the main chamber walls. The simulations matched the spatial D_α intensity distribution in the divertor, as well as in the inner and outer midplane SOL. The asymmetric emission profiles of D_α, CII, and CIII in the inner and outer divertor legs were consistently reproduced, provided the effects of $\mathbf{B}x\nabla B$ and $\mathbf{E}x\mathbf{B}$ drifts were included in the UEDGE simulations. In plasmas with the ion $\mathbf{B}x\nabla B$ into the divertor, the inner divertor leg is at higher density and lower temperature than the outer, which facilitates stronger fueling from the high-field side of the divertor X-point region.

The poloidal distribution of carbon ions along the inner separatrix peaked toward the divertor X-point, which suggests that the source of this carbon is in the divertor region. If this is the case, improved impurity screening by a more robust divertor plasma may be feasible in future fusion devices. Measured carbon emission profiles in the divertor were matched with UEDGE using physical and chemical sputtering yields published in [23]. Flow reversal in the divertor away from the target was predicted by the codes and can lead to enhanced leakage of carbon ions out of the divertor into the inner main SOL.

Acknowledgment

References

[1]   MAHDAVI, M.A., *et al.*, Phys. Plasmas **10** (2003) 3984.
[2]   OSBORNE, T.H., *et al.*, Plasma Phys. and Contr. Fusion **42** (2000) A175.
[3]   JET TEAM (prepared by R.D. MONK), Nucl. Fusion **39** (1999) 1751.
[4]   ALLEN, S.L., *et al.*, J. Nucl. Mater. **266-269** (1999) 168.
[5]   TAKENAGA, H., *et al.*, Nucl. Fusion **41** (2001) 1777.
[6]   McCRACKEN, G.M., *et al.*, Nucl. Fusion **39** (1999) 41.
[7]   STRACHAN, J.D., *et al.*, Nucl. Fusion **43** (2003) 992.
[8]   WEST, W.P., *et al.*, J. Nucl. Mater. **313-316** (2003) 1211.
[9]   FEDERICI, G., *et al.*, J. Nucl. Mater. **313-316** (2003) 11.
[10]   LABOMBARD, B., *et al.*, Phys. Plasmas **8** (2001) 2107.
[11]   BOEDO, J.A., *et al.*, Phys. Plasmas **8** (2001) 4826.
[12]   FENSTERMACHER, M.E., *et al.*, Rev. Sci. Instrum. **70** (1997) 974.
[13]   GROTH, M., *et al.*, Rev. Sci. Instrum. **74** (2003) 2064.
[14]   COLCHIN, R.J., *et al.*, Rev. Sci. Instrum. **74** (2003) 2068.
[15]   WATKINS, J.G., *et al.*, J. Nucl. Mater. **241-243** (1997) 645.
[16]   WATKINS, J.G., *et al.*, Rev. Sci. Instrum. **63** (1992) 4728.
[17]   ZENG, L., *et al.*, Rev. Sci. Instrum. **72** (2001) 320.
[18]   CARLSTROM, T.N., *et al.*, Rev. Sci. Instrum. **63** (1992) 4901.
[19]   ROGNLIEN, T.D., *et al.*, J. Nucl. Mater. **196-198** (1992) 347.
[20]   HEIFETZ, D.B., et al., J. Comp. Phys. **46** (1982) 309.
[21]   GREENWALD, M., *et al.*, Nucl. Fusion **28** (1988) 2199.
[22]   ROGNLIEN, T.D., *et al.*, J. Nucl. Mater. **266-269** (1999) 654.
[23]   DAVIS, J.W., *et al.*, J. Nucl. Mater. **241-243** (1997) 37.
[24]   NEUHAUSER, J., *et al.*, Nucl. Fusion **24** (1984) 39.
[25]   OWEN, L.W., *et al.*, J. Nucl. Mater. **290-293** (2001) 464.
[26]   COLCHIN, R.J., *et al.*, J. Nucl. Mater. **313-316** (2003) 806.
[27]   GROTH, M. *et al.*, J. Nucl. Mater. **313-316** (2003) 1071.
[28]   PETRIE, T.W., *et al.*, J. Nucl. Mater. **313-316** (2003) 834.